Process Mineralogical Characterisation of Historical Tin Mine Wastes for Recovery of In, Sn, Sb, W, and Bi

Steve Jason Chingwaru[1]; Olivia Mejías[1]; Rosie Blannin[1]; Nathan Fox[1,] Anita Parbhakar-Fox[1]

1. W. H. Bryan Mining & Geology Research Centre, Sustainable Minerals Institute, The University of Queensland, QLD 4068, Australia

Abstract

Demand for critical elements is increasing, yet supply remains constrained by by-product dependence and declining discoveries. Reprocessing historical mine waste offers a sustainable alternative. This study evaluates legacy tailings from the Herberton Sn–W–Sb–Bi mineral field (Australia) using a process mineralogy framework. A multi-scale workflow integrating bulk geochemistry, automated mineralogy, LA-ICP-MS, and XFM synchrotron mapping was applied to quantify mineral associations and element deportment. Results show significant enrichment (up to 1,155 ppm In, 81,600 ppm Sn, 53,600 ppm Sb, 11,650 ppm W, and 3,640 ppm Bi). Deportment varies systematically: lower-grade samples are dominated by secondary Fe–Sn–Pb–Sb phases, whereas higher-grade samples host elements in primary sulphides and Sn–W oxides. Gravity recovery modelling predicts high recoveries, with limitations linked to fine grain size, silicate locking, and secondary mineralisation. These results demonstrate a robust pathway for sustainable recovery of critical elements from legacy mine waste.

1. Introduction

Critical elements underpin electronics, renewable-energy systems and advanced defence technologies, yet their supply remains vulnerable to geopolitical concentration, by-product dependence and declining discovery rates (Arrobas *et al.,* 2023; Jowitt *et al.*, 2018). Indium (In), tin (Sn), antimony (Sb), tungsten (W) and bismuth (Bi) appear on multiple national and international critical-mineral lists, and In and Bi are recovered almost exclusively as by-products of Zn, Cu, Sn, Pb and W processing (Deady *et al.,* 2022; Nassar *et al.,* 2015). With China accounting for more than 80% of global W production and a majority of Sb, In and Bi output (U.S. Geological Survey, 2025), primary mining alone is unlikely to secure supply, and reprocessing legacy mine waste offers an on-surface option that also reduces long-term environmental liabilities.

Historical mine wastes are, however, mineralogically complex. Past processing, deposition conditions and subsequent weathering have produced heterogeneous materials in which

target elements may be locked in fine-grained primary minerals, dispersed through secondary oxyhydroxides, sulphates and arsenates, or hosted at scales below the resolution of routine analysis (Jamieson *et al.,* 2015). Predicting how such material will respond to physical or chemical separation therefore requires a process mineralogy approach that links mineral identity, chemistry, grain size, liberation and texture to element deportment.

The Herberton Mineral Field (HMF) in north Queensland hosts granite-related Sn–W–In–Sb systems (Figure 1a) that were mined for more than a century, ceasing in 1987 (Kumar et al., 2024; Walshe et al., 2011). Indium, Sb and Bi were never targeted, so their legacy tailings and waste rock represent a potentially overlooked resource (Fox *et al.,* 2016; Lottermoser & Ashley, 2006). This extended abstract integrates bulk geochemistry, automated mineralogy (MLA), mineral-scale LA-ICP-MS and synchrotron X-ray fluorescence microscopy (XFM) to define the deportment of In, Sn, Sb, W and Bi across eight HMF waste sites, and uses the results in first-order gravity-separation modelling to identify the mineralogical controls on recovery.

2. Material Preparation and Characteristics

A total of 290 samples were collected from eight HMF sites(Figure 1a): Jumna, Herberton and Irvinebank (tailings, sampled by auger to 6–9 m depth) and Copper Firing Line, Baal Gammon, Confederation, Montalbion and Victoria (waste rock, collected by surface grab sampling; Figure 1a). The sampling strategy captured the physical and mineralogical heterogeneity of each waste type rather than a tonnage-proportional composite. Samples were dried at 60 °C, deagglomerated or crushed to 70% passing 2 mm, subsampled and pulverised to 85% passing 75 µm for geochemical analysis, with aliquots retained for mineralogical work.

Bulk geochemistry was determined at ALS Brisbane by four-acid digestion ICP-MS (ME-MS61) and lithium borate fusion ICP-MS (ME-MS81) for refractory elements including Sn and W. Principal component analysis (PCA) of the log-transformed, standardised dataset (n = 290) defined three geochemical clusters (Figure 2): a low-grade cluster dominated by the silicate-rich tailings of Jumna, Herberton and Irvinebank; a Pb–Ag high-grade cluster (Montalbion, Copper Firing Line); and a Cu–Zn high-grade cluster (Baal Gammon, Confederation, Victoria). Between two and ten samples per site, selected for elevated Bi, Sb, Sn, In or W, were then characterised by mineralogy (n = 40).

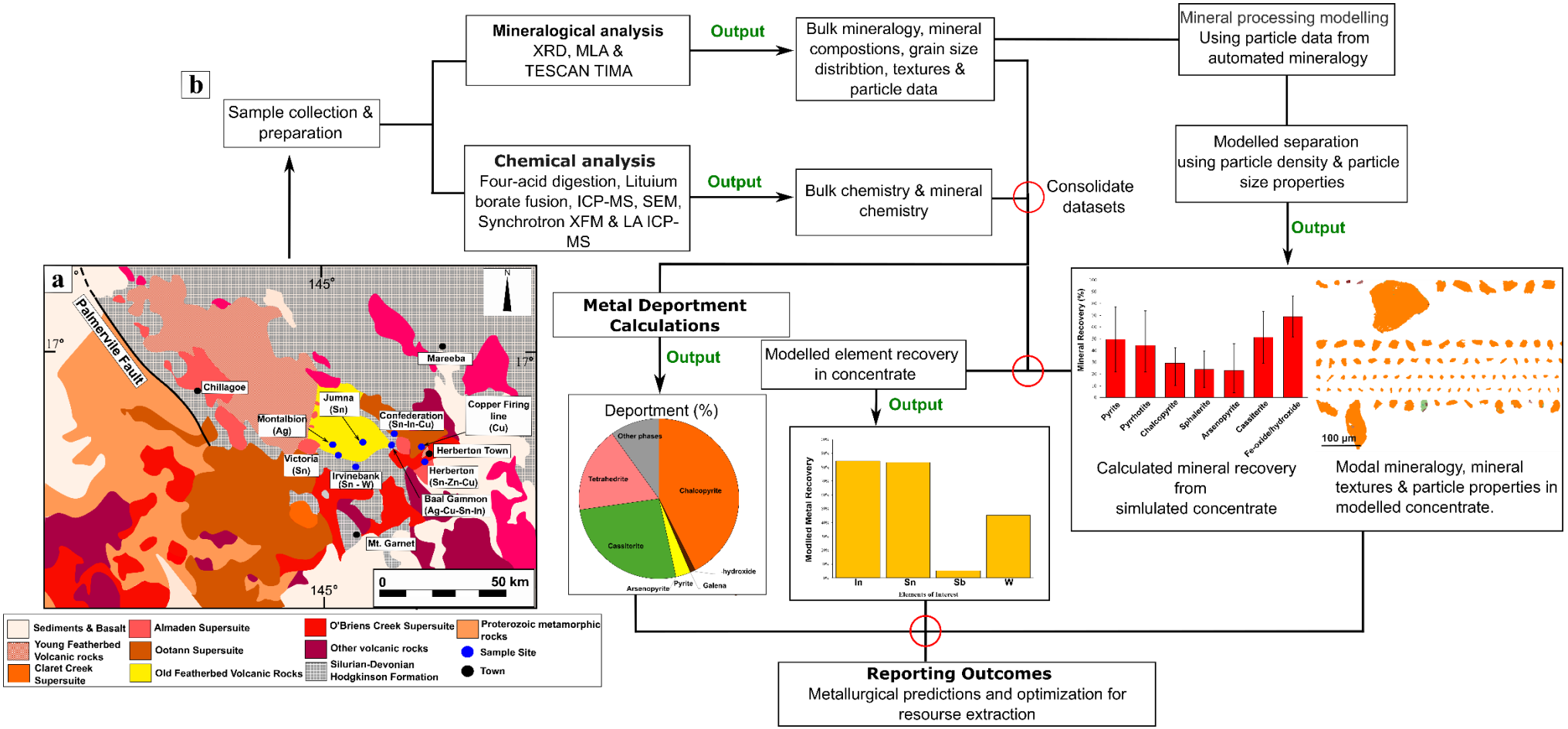

Figure 1: (**a**) Simplified geological map of the HMF showing volcanic rocks, granitoids, sediments, towns, historical mine-waste sample sites, and primary commodities mined modified after Kumar *et al.* (2024). (**b**) Methodological flowchart integrating mineralogical and chemical analyses to predict metallurgical recovery pathways for In, W, Sn, Sb, and Bi. Chingwaru *et al.*(2024).

3. Methodology

The summary of the methodology flowsheet is displayed in Figure 1b. Unsized 5–10 g aliquots were mounted as vertical sections in carbon-doped epoxy, polished to 1 µm and carbon-coated. Modal mineralogy, particle size and liberation (n = 40) were measured with the UQ Mineral Liberation Analyser (MLA; Quanta 600 SEM, 25 kV, 5 nA, 0.9 µm per pixel). In situ mineral chemistry was obtained from 802 LA-ICP-MS spots across 22 mounts using 193 nm excimer and ArF laser systems coupled to Agilent quadrupole ICP-MS instruments at the University of Adelaide and CODES (University of Tasmania), calibrated against STDGL3, GSD-1G and BCR-2G and processed in LADR. Fine-grained Bi, Sb, W and Sn phases below the LA-ICP-MS spot size were mapped semi-quantitatively with a TESCAN Integrated Mineral Analyser (TIMA) at AXT, Perth.

Synchrotron X-ray fluorescence microscopy (XFM) was used to map the micron-scale distribution of In, Bi and Fe in representative 400 µm-thick polished sections, providing element-specific information beyond the resolution of backscatter-based MLA. Maps were acquired on the XFM beamline at the Australian Synchrotron, Clayton, Australia (Howard *et al.,* 2020), using a monochromatic 28.5 keV incident beam and a 384-element Maia detector. Overview scans were collected at 20 µm pixel resolution, with selected regions mapped at 2 µm resolution. Data were processed using GeoPIXE (Ryan *et al.*, 2014) and registered to corresponding MLA particle maps, enabling fluorescence hotspots to be linked to individual mineral grains and trace-element hosts not discernible in backscatter images to be identified (Figure 5).

Elemental deportment was calculated for each site by mass balance (modified after Chingwaru *et al.,* 2024):

$$\text{Deportment (\%)} = \frac{\text{Mineral contribution (ppm)} \times \text{mineral abundance}}{\text{Bulk concentration (ppm)}} \times 100 \quad (1)$$

where the mineral contribution is the mean LA-ICP-MS concentration of the element in that mineral, mineral abundance is the MLA modal proportion, and bulk concentration is the digestion assay. Summed host contributions give the assigned fraction; the remainder (100 minus assigned) is the unassigned fraction. Propagated analytical uncertainty averages ~5% (range 3–9%; ISO/IEC, 2021). Theoretical gravity recovery was modelled by classifying MLA particles as concentrate or tailings using density and size cut-offs (particles below 2.90 g/cm³ and 20 µm treated as poorly amenable to gravity separation), then calculating recovery as:

$$\text{Element Recovery (\%)} = \left(\frac{C \times M_c}{M_f}\right) \times 100 \quad (2)$$

where C is the concentrate weight fraction, Mc is the element concentration in the concentrate (mineral proportion × LA-ICP-MS grade) and Mf is the bulk feed grade. Total recovery sums contributions across minerals. The unassigned fraction is implicitly treated as unrecovered, so modelled values are comparative indicators of mineralogical constraints and not predictions of plant performance.

4. Results

4.1 Bulk geochemistry and geochemical clusters

The 290 samples are strongly enriched in target elements relative to average crustal abundances (Figure 3), with maximum concentrations of 1,155 ppm In, 81,600 ppm Sn, 53,600 ppm Sb, 11,650 ppm W and 3,640 ppm Bi. Mean As and Pb concentrations are approximately 7,994 and 6,686 ppm, respectively. Enrichment varies by site, with Irvinebank exhibiting the highest mean Sn (39,463 ppm) and W (4,009 ppm) concentrations, Montalbion the highest mean Sb (8,067 ppm), and Confederation the highest mean In (262 ppm) and Bi (427 ppm) concentrations.

PCA; 49% of total variance explained; Figure 2 distinguished three geochemical clusters: silicate-rich, low-grade tailings (n = 166), Pb–Ag-rich sulphidic wastes (n = 31) and Cu–Zn-rich wastes (n = 92). These clusters provide a geochemical framework for interpreting the subsequent mineralogical results. Comparison with typical ore-grade ranges (Figure 3) indicates that In and Bi concentrations fall within these ranges across all three clusters. Sn concentrations reach typical ore-grade ranges in the low-grade and Cu–Zn clusters, whereas Sb reaches these ranges only in the Pb–Ag cluster. W concentrations remain below typical ore-grade ranges across all three clusters.

4.2 Mineralogy and particle characteristics

Mineralogy and particle size vary markedly between clusters (Figure 4). The low-grade cluster (Figure 4a) is fine-grained (P_{80} 125–355 µm) and silicate-dominated (87–93 wt%), with 0.4–0.6 wt% primary sulphides, 0.3–2 wt% cassiterite and trace wolframite and bismuthinite. Fe-oxides/hydroxides account for 3–4 wt%, alongside secondary phases including schwertmannite, scorodite and Fe–Sn–Pb–Sb oxides.

The Cu–Zn cluster (Figure 4b) is coarser (P_{80} ~500–1,200 µm) and sulphide-rich (24–51 wt%), with distinct site-specific assemblages. Baal Gammon is dominated by pyrrhotite (29 wt%), chalcopyrite (13 wt%) and arsenopyrite (9 wt%); Confederation by chalcopyrite (15 wt%), pyrrhotite (11 wt%), pyrite (4 wt%) and stannite (3 wt%); and Victoria by sphalerite (13 wt%), pyrite (5 wt%) and galena (4 wt%). Other sulphides occur in minor proportions. Accessory

phases include cassiterite (0.3–2 wt%), Fe-oxyhydroxides (0.1–2 wt%), minor rutile/ilmenite and wolframite, and sulphates (0.2–0.5 wt%). Secondary phases are particularly abundant at Confederation and Victoria, including schwertmannite (≤2 wt%) and Fe–Pb–Sb–Sn oxides (0.2–5 wt%). Scorodite reaches 29 wt% at Confederation but is lower at Victoria (0.3 wt%). Bismuthinite is rare (<0.1 wt%).

The Pb–Sb high-grade cluster (Figure 4c) shows strong site-dependent variation. Montalbion contains tetrahedrite (7 wt%), boulangerite (1 wt%) and galena (2 wt%), whereas these minerals occur at <1 wt% and particle sizes <20 μm at Copper Firing Line. Bi-bearing minerals are rare (<0.02 wt%). Oxides/hydroxides account for 2–4 wt%, while cassiterite (0.1–0.6 wt%), wolframite (<0.2 wt%) and rutile/ilmenite (<0.4 wt%) are minor. Secondary phases include schwertmannite (1–3 wt%), scorodite (~0.1 wt%), sulphates (0.1–2 wt%) and Fe–Pb–Sb–Sn oxides (0.1–2 wt%).

4.3 Element Deportment

MLA- and LA-ICP-MS-derived deportment (Figure 5) reveals distinct element-hosting patterns across the three geochemical clusters. In the low-grade cluster (Figure 5a), In is hosted predominantly by Fe-oxides/hydroxides (61%), with an additional 18% in scorodite at Herberton. Sn occurs mainly in cassiterite (70%) and Fe–Sn–Pb–Sb oxides (21%), whereas Sb is distributed between Fe-oxides/hydroxides (37–86%) and boulangerite, tetrahedrite, scorodite and Fe–Sn–Pb–Sb oxides (collectively 43%). W is hosted by wolframite (45%), cassiterite (24%) and Fe-oxides/hydroxides (20%). Bi occurs mainly in Fe-oxides (37%) and bismuthinite (33%), with 11% as native Bi.

In the Cu–Zn cluster (Figure 5b), In is hosted by chalcopyrite (34%; Figure 6a), sphalerite (19%) and scorodite (24%; Figure 6b), with a further 8% in pyrrhotite. Sn occurs predominantly in cassiterite (66%) and Fe–Sn–Pb–Sb oxides (21%). Sb is distributed among galena (30%), boulangerite (21%), cassiterite and pyrite (11% each), and scorodite (8%). W is hosted mainly by wolframite (72%) and cassiterite (18%), while Bi occurs predominantly in bismuthinite (62%), followed by scorodite (17%; Figure 6b) and native Bi (16%).

In the Pb–Ag cluster (Figure 5c), In occurs mainly in chalcopyrite (43%; Figure 6a), cassiterite (18%), pyrite (13%) and tetrahedrite (12%), with 5% in scorodite. Sn is divided between cassiterite (48%) and Fe–Sn–Pb–Sb oxides (46%). Sb is hosted predominantly by tetrahedrite (70%), with smaller contributions from cassiterite (12%), Fe–Sn–Pb–Sb oxides (9%) and galena (6%). W occurs mainly in wolframite (65%), followed by pyrite (14%) and cassiterite (9%). Bi is hosted by bismuthinite (57%), scorodite (20%; Figure 5b) and pyrite (9%).

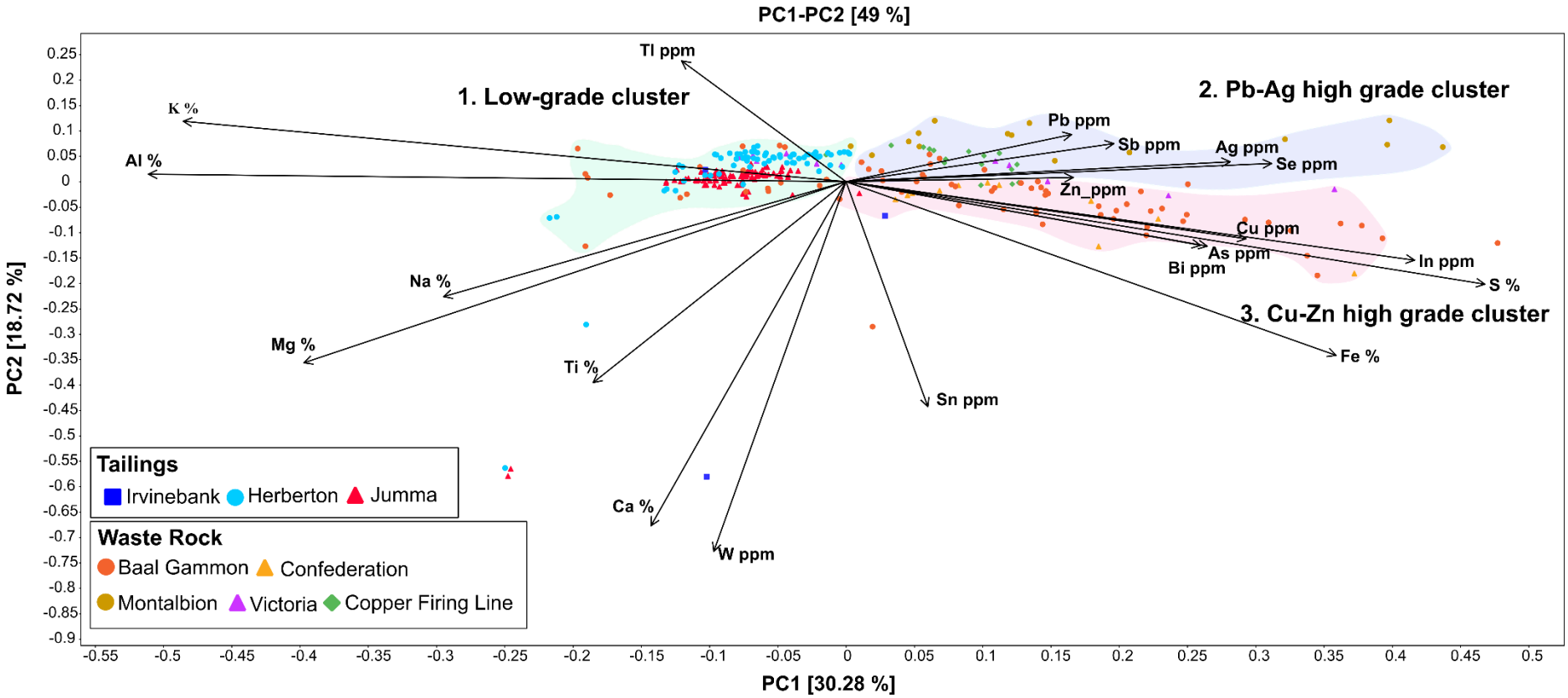

Figure 2: PCA of bulk geochemical data (n = 290) from eight sites showing three clusters: **1**) low-grade, **2**) Pb–Ag high-grade, **3**) Cu–Zn high-grade. Black vectors indicate element correlations and enrichments.

Deportment remains partly unresolved, with 1–13% unassigned (Figure 5). TIMA mapping identified additional fine-grained or sub-pixel hosts, including native Bi inclusions in quartz, Bi–Sb secondary oxides, Sn–Sb-bearing stannite rims and ferberite grains, several of which are smaller than 20 µm. These features likely account for part of the unassigned fraction and highlight the limitations of automated mineralogy and LA-ICP-MS spot-scale analysis in resolving fine-grained element hosts. Further XFM analysis could help constrain their distribution at finer spatial scales and lower detection limits, although this was beyond the scope of the present study.

4.4 Modelled gravity recovery and loss pathways

Modelled recoveries (Figure 7) reflect these host mineralogies, grain sizes and liberation states. Low-grade samples give 22–85% In, 53–65% Sn, 26–62% Sb, 14–37% W and 28–48% Bi. Higher recoveries are modelled for the Pb–Ag cluster (In 61–98%, Sn >90%, Sb 61–91%, W 20–77%, Bi 26–51%) and the Cu–Zn cluster (In 41–74%, Sn >70%, Sb 73–84%, W 50–91%, Bi 38–53%). Across all samples, the modelled range is 22–85% In, 53–99% Sn, 26–91% Sb, 13–91% W and 26–51% Bi.

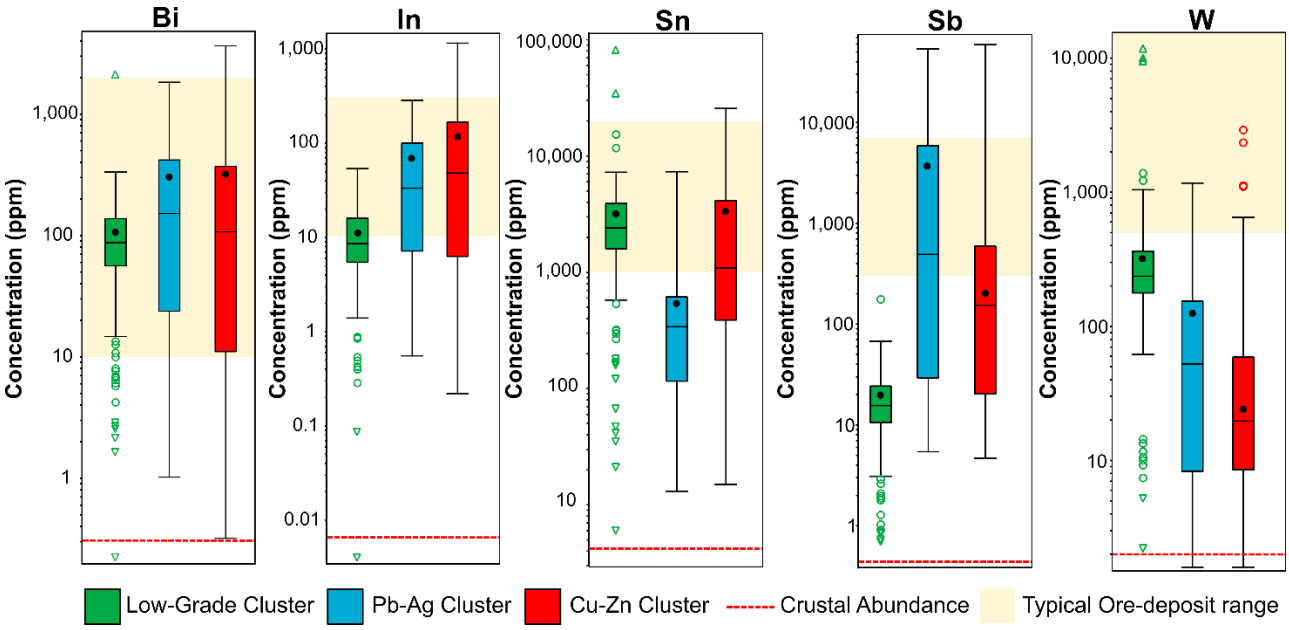

Figure 3: Boxplot of enriched element concentrations in defined geochemical clusters from the HMF mine waste samples (n = 290) determined by four-acid digestion.

Inspection of the modelled tailings particle by particle (Figure 8) identifies the main loss pathways: sulphides, wolframite, cassiterite and bismuthinite occluded in quartz and feldspar (Figure 8a–d); fine secondary Fe–Pb–Sb–Sn oxides intergrown with silicates (Figure 8e); and liberated but very fine (~10 µm) wolframite, bismuthinite, tetrahedrite, chalcopyrite and sphalerite (Figure 8f–h). Examples include Montalbion (tetrahedrite and chalcopyrite <10 µm),

Victoria (In-bearing sphalerite intergrown with silicates, In recovery 41%) and Baal Gammon (fine arsenopyrite hosting 65% of Sb, Sb recovery 50%).

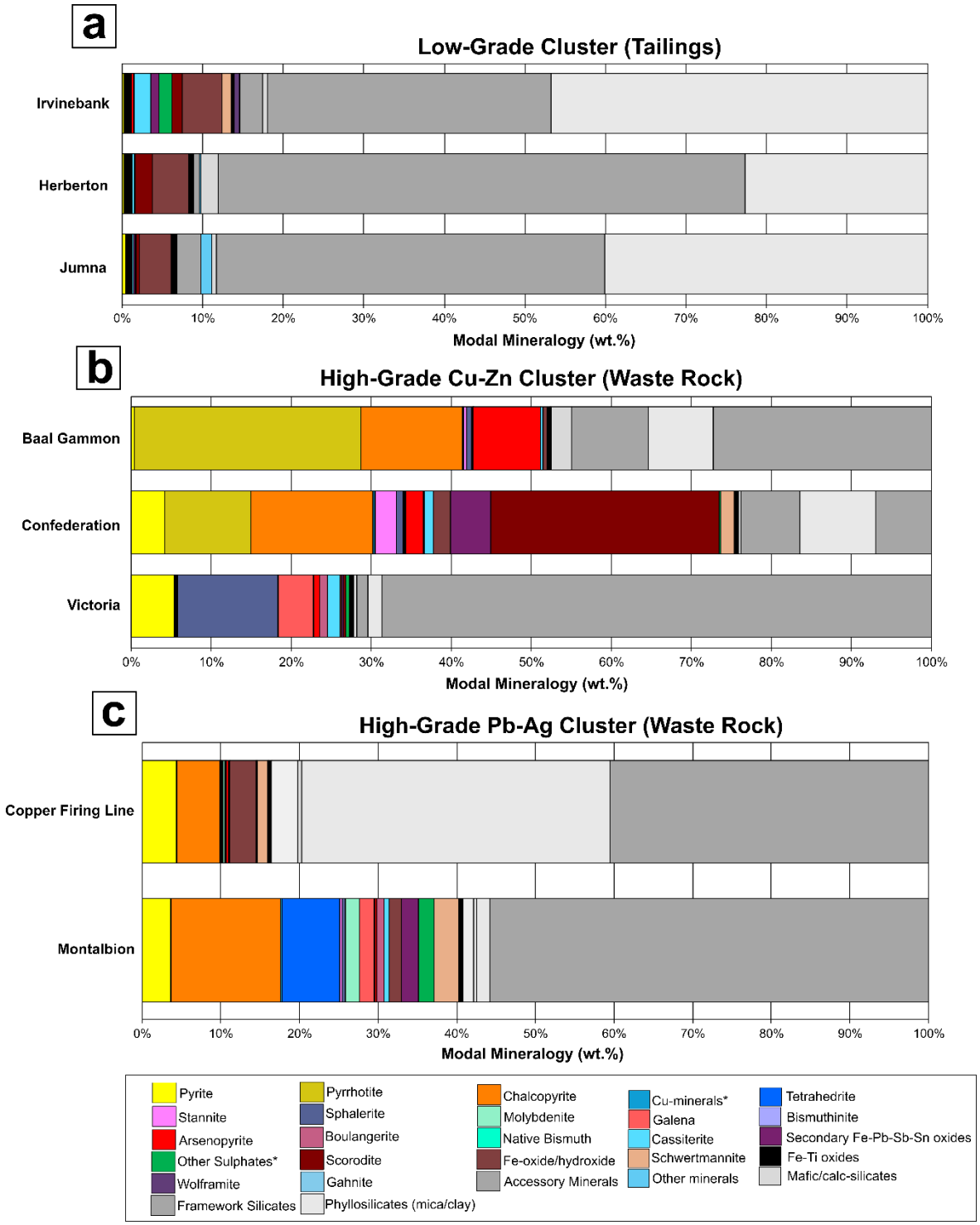

Figure 4 : Average mineralogical composition of the HMF mine-waste samples by geochemical cluster (n = 40), determined by MLA.

5. Discussion

From a process mineralogy perspective, five mineral-scale parameters control the response of these wastes: host-mineral identity and density, mineral chemistry (trace-element grade of each host), grain size and liberation, mineral association with silicate gangue and secondary rims, and the proportion of each element that cannot yet be assigned to a host. Combining MLA modal data with LA-ICP-MS chemistry, and constraining the finest hosts with XFM and TIMA, allows these parameters to be carried into recovery modelling and flowsheet selection before any test work is done.

The results show that deportment, not bulk grade, governs recoverability. In the low-grade tailings, weathering has redistributed In, Sb and Bi into fine-grained Fe-oxyhydroxides, schwertmannite and scorodite, which are low-density and intergrown with silicate gangue and are therefore poorly amenable to gravity separation. Physical pre-concentration of cassiterite, wolframite and liberated sulphides may be feasible, but a substantial proportion of In, Sb and Bi would require hydrometallurgical treatment. In the coarser, sulphide-rich high-grade wastes, target elements are held in dense, liberated primary minerals that favour gravity and flotation, and modelled losses are controlled by grain size and silicate locking rather than by host mineralogy.

Secondary hosts also impose process constraints. Schwertmannite and Fe-oxyhydroxides release In, Bi and Sb on acidic or reductive dissolution but add Fe to solution, raising reagent demand (Bigham *et al.*, 1990; Bolan *et al.*, 2022). Scorodite, abundant at Confederation (28.8 wt%), is stable only under mildly acidic, oxidising conditions and can release As under more aggressive acidic or reducing conditions (Bluteau & Demopoulos, 2007; Langmuir *et al.,* 2006; Nazari *et al.,* 2017). Because these phases are metastable, As mobilisation must be considered when selecting and designing leaching routes. Primary sulphides such as arsenopyrite and galena, by contrast, weather oxidatively, so tailings from processing high-grade wastes will need acid-rock-drainage management.

XFM adds a spatial dimension to the standard MLA–LA-ICP-MS workflow. Whereas MLA and LA-ICP-MS quantify mineral abundance and mineral chemistry separately and combine them by mass balance, XFM maps trace-element distributions directly within the particles, making it possible to test whether In and Bi are lattice-bound in sulphides or hosted in Fe-rich secondary coatings and cements, and to detect hosts below the ~20 µm LA-ICP-MS spot size that currently populate the unassigned fraction (Fougerouse *et al.,* 2023; Stromberg *et al.*, 2019). In a process context, these distinctions determine whether an element will follow its host mineral into a gravity or flotation concentrate or remain with the gangue.

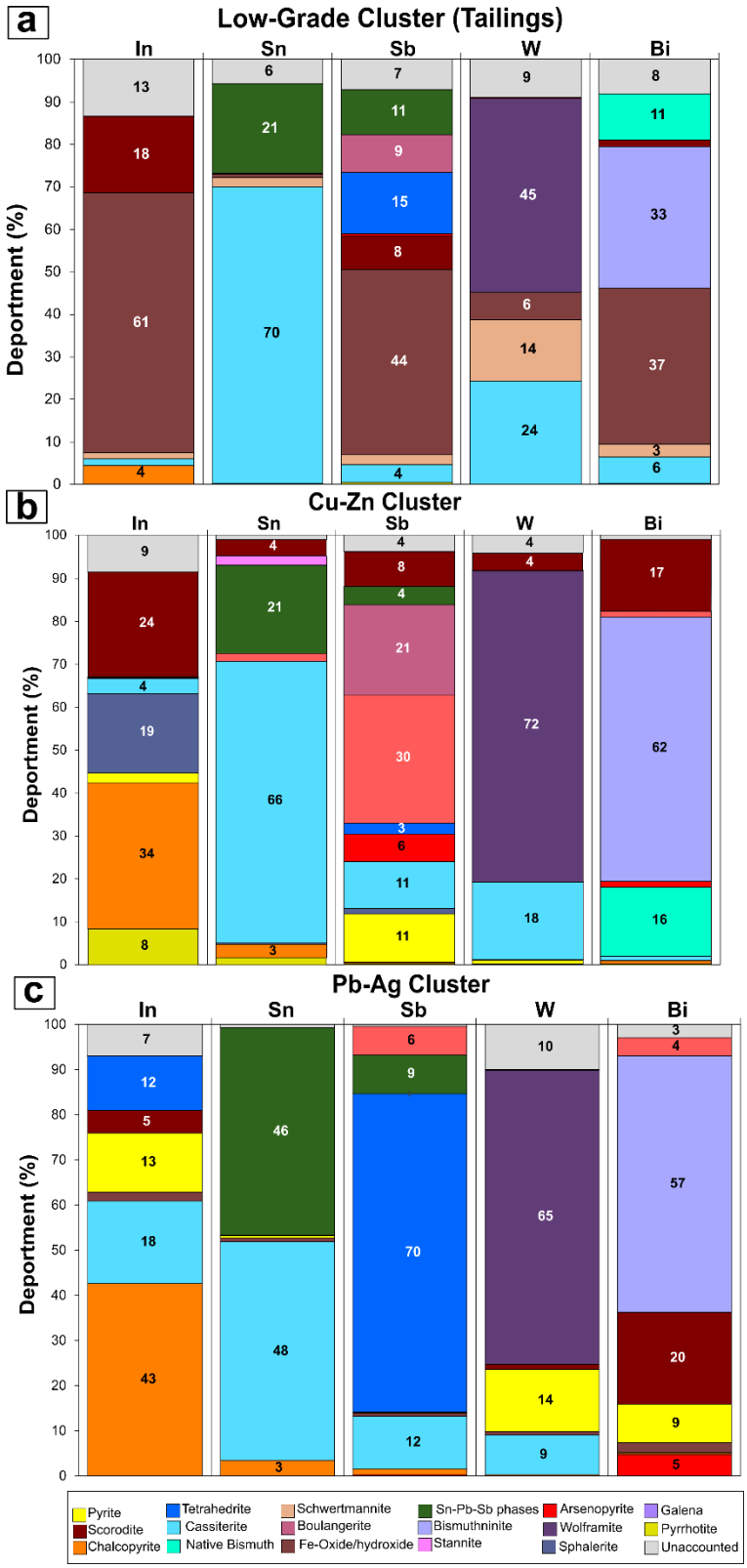

Figure 5: Percentage bar charts showing the deportment of In, Sn, Sb, W, and Bi within clusters: (**a**) low-grade sites – Jumna, Herberton, and Irvinebank; (**b**) Pb–Ag high-grade sites – Montalbion & Copper Firing Line; (c) Cu–Zn high-grade sites – Victoria, Confederation, & Baal Gammon.

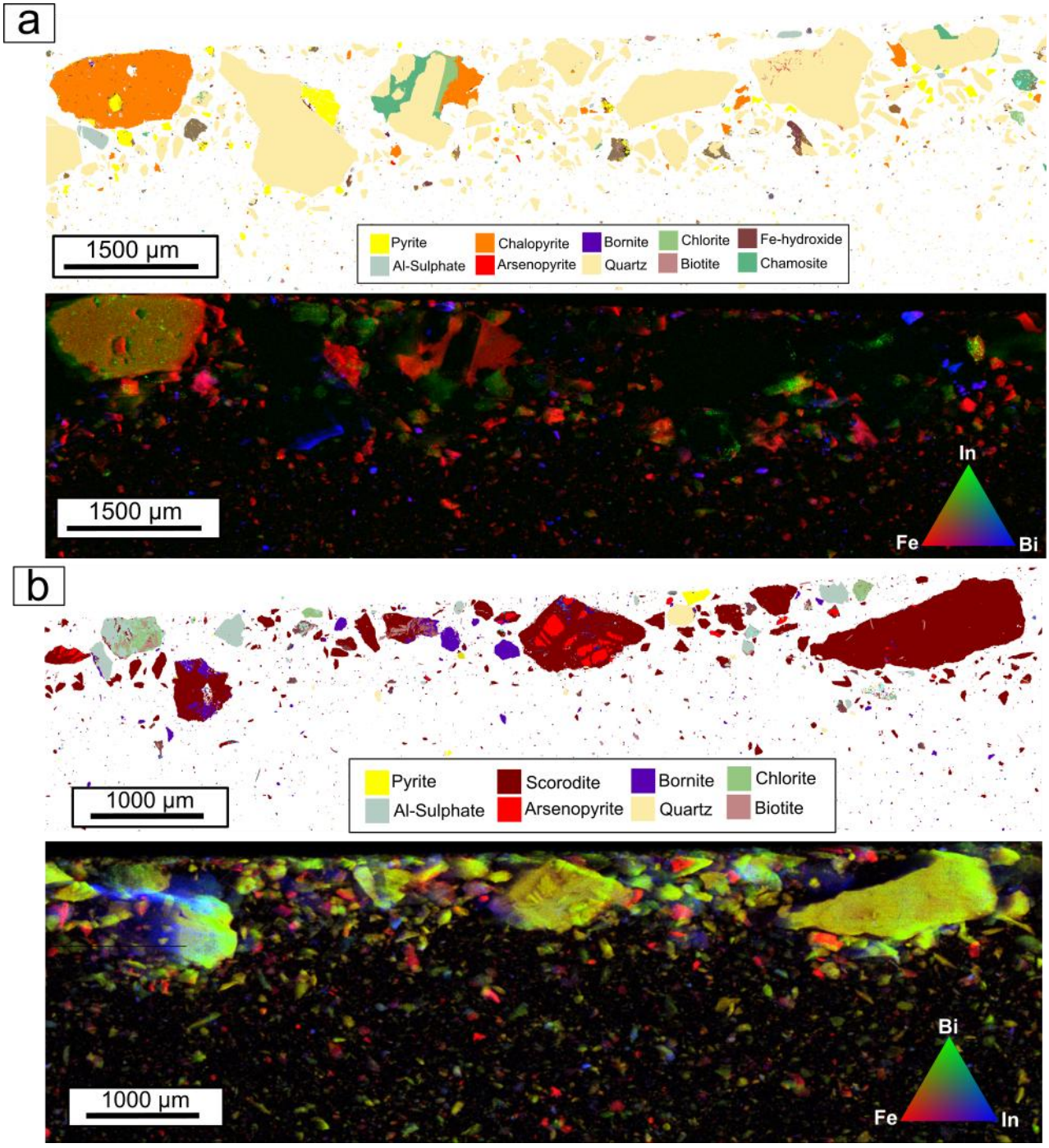

Figure 6: Particle maps derived from automated mineralogy, alongside corresponding synchrotron XFM elemental maps for Bi, Fe and In, showing (**a**) material dominated by primary minerals, including pyrite and chalcopyrite, and (**b**) material dominated by secondary minerals, exemplified by scorodite.

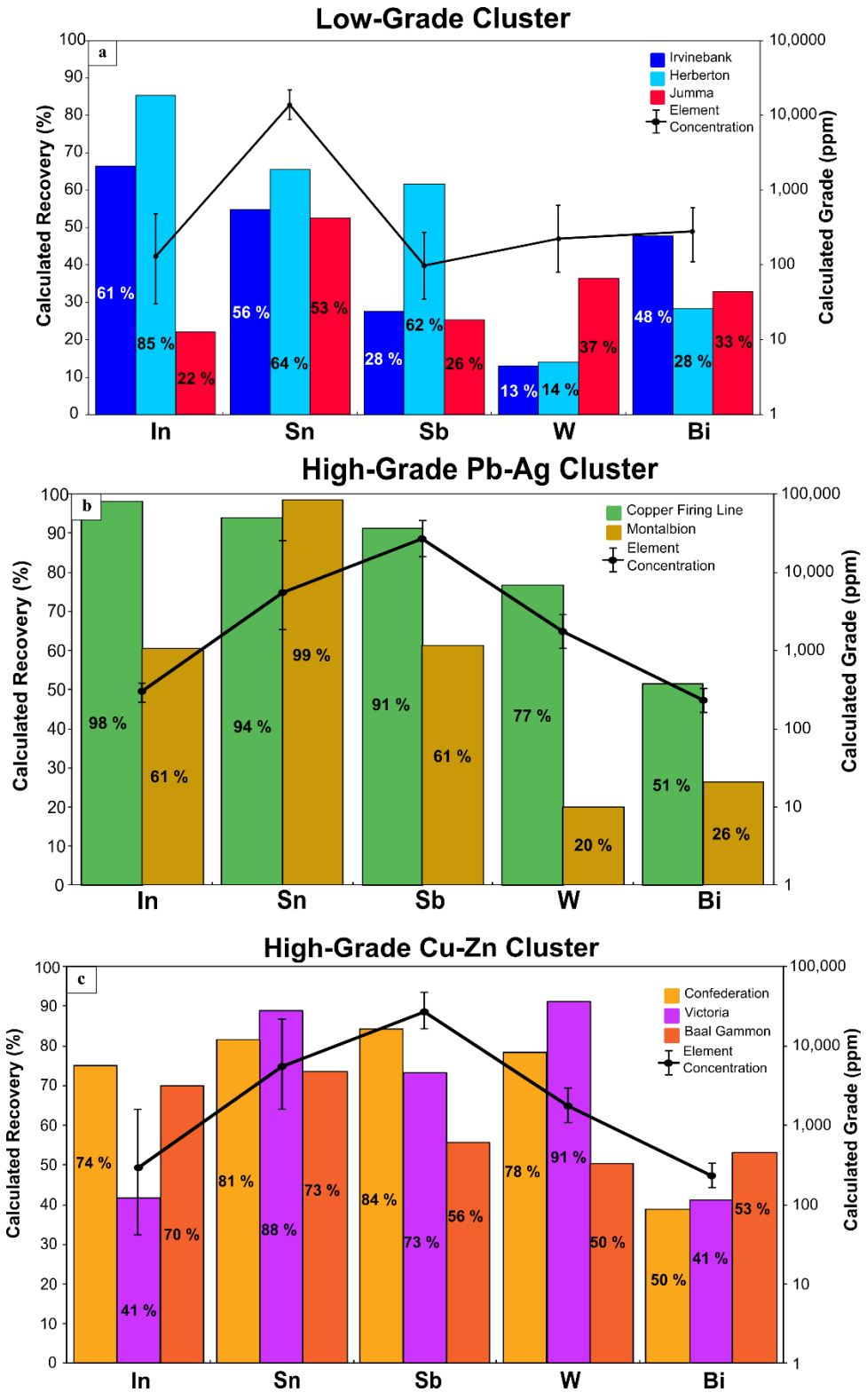

Figure 7:Average theoretical recovery of In, Sn, Sb, W and Bi by cluster based on density separation (bar charts). Line graphs show average calculated concentrations ±1 SD.

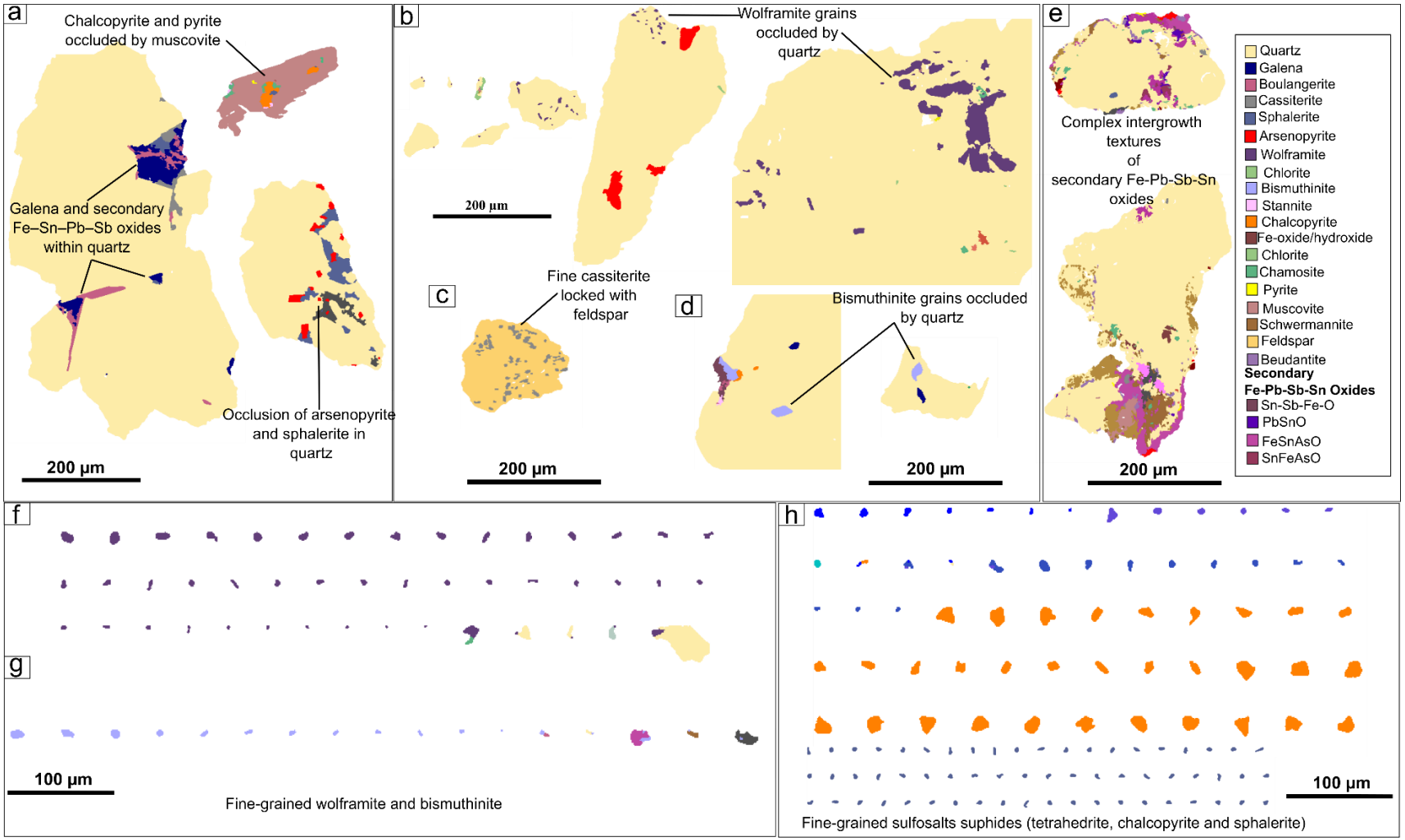

Figure 8: Example pixel maps of MLA-modelled tailings highlighting potential loss pathways: (**a**) base-metal/Fe sulphides occluded by silicates, (**b**) wolframite occluded by quartz, (**c**) cassiterite occluded by feldspar, (**d**) bismuthinite occluded by quartz, (**e**) secondary Fe–Pb–Sb–Sn oxides intergrown with silicates, (**f**) fine wolframite, (**g**) fine bismuthinite, and (**h**) very fine tetrahedrite, chalcopyrite, sphalerite and secondary oxides reporting to tailings.

6. Conclusion

Process mineralogy of legacy waste from eight Herberton sites shows that the potential to recover In, Sn, Sb, W and Bi is controlled by host mineralogy, grain size and texture. Low-grade tailings host 60–97% of target elements in secondary oxyhydroxides and arsenates, whereas high-grade wastes host more than 60% in primary sulphides and Sn–W oxides. Gravity modelling indicates 22–85% In, 53–99% Sn, 26–91% Sb, 13–91% W and 26–51% Bi, with losses driven by fine grain size, silicate locking and secondary mineralisation. Synchrotron XFM complements MLA and LA-ICP-MS by revealing the spatial residence of In and Bi and offers a pathway to resolve the unassigned fraction. These findings support a site-specific gravity–flotation–leaching strategy and prioritise metallurgical validation, with As and Pb fate treated as integral to process design.

References

Arrobas, D. L. P., Drexhage, J. R., Fabregas Masllovet, T. P., Hund, K. L., & Laing, T. J. (2023). *Minerals for Climate Action: The Mineral Intensity of the Clean Energy Transition*. World Bank. http://documents.worldbank.org/curated/en/099052423172525564

Bigham, J. M., Schwertmann, U., Carlson, L., & Murad', E. (1990). A poorly crystallized oxyhydroxysulfate of iron formed by bacterial oxidation of Fe(I1) in acid mine waters. *Geochimica et Cosmochimica Acta*, *54*, 2743–2758.

Bluteau, M.-C., & Demopoulos, G. P. (2007). The incongruent dissolution of scorodite—Solubility, kinetics and mechanism. *Hydrometallurgy*, *87*(3–4), 163–177. https://doi.org/10.1016/j.hydromet.2007.03.003

Bolan, N., Kumar, M., Singh, E., Kumar, A., Singh, L., Kumar, S., Keerthanan, S., Hoang, S. A., El-Naggar, A., Vithanage, M., Sarkar, B., Wijesekara, H., Diyabalanage, S., Sooriyakumar, P., Vinu, A., Wang, H., Kirkham, M. B., Shaheen, S. M., Rinklebe, J., & Siddique, K. H. M. (2022). Antimony contamination and its risk management in complex environmental settings: A review. *Environment International*, *158*, 106908. https://doi.org/10.1016/j.envint.2021.106908

Chingwaru, S. J., Tadie, M., & Von der Heyden, B. (2024). Characterizing low-grade refractory gold ores using automated mineralogy coupled with LA ICP-MS. *Minerals Engineering*, *210*(May), 108674. https://doi.org/10.1016/j.mineng.2024.108674

Deady, E., Moon, C., Moore, K., Goodenough, K. M., & Shail, R. K. (2022). Bismuth: Economic geology and value chains. *Ore Geology Reviews*, *143*, 104722. https://doi.org/10.1016/j.oregeorev.2022.104722

Fougerouse, D., Cugerone, A., Reddy, S. M., Luo, K., & Motto-Ros, V. (2023). Nanoscale distribution of Ge in Cu-rich sphalerite. *Geochimica et Cosmochimica Acta*, *346*, 223–230. https://doi.org/10.1016/j.gca.2023.02.011

Fox, N., Parbhakar-Fox, A., & Lottermoser, B. G. (2016). Critical and Deleterious Metal Deportment in Sulfidic Waste Rocks, Baal Gammon, north queensland. *The Third AusIMM International Geometallurgy Conference*. AusIMM International Geometallurgy Conference, Perth, Australia.

Howard, D. L., De Jonge, M. D., Afshar, N., Ryan, C. G., Kirkham, R., Reinhardt, J., Kewish, C. M., McKinlay, J., Walsh, A., Divitcos, J., Basten, N., Adamson, L., Fiala, T., Sammut, L., & Paterson, D. J. (2020). The XFM beamline at the Australian Synchrotron. *Journal of Synchrotron Radiation*, *27*(5), 1447–1458. https://doi.org/10.1107/S1600577520010152

ISO/IEC. (2021). *Uncertainty of measurement—Part 6: Developing and using measurement models*. ISO (the International Organization for Standardization) and IEC (the International Electrotechnical Commission). https://www.iso.org/obp/ui/#iso:std:iso-iec:guide:98:-6:ed-1:v1:en

Jamieson, H. E., Walker, S. R., & Parsons, M. B. (2015). Mineralogical characterization of mine waste. *Applied Geochemistry*, *57*, 85–105. https://doi.org/10.1016/j.apgeochem.2014.12.014

Jowitt, S. M., Mudd, G. M., Werner, T. T., Weng, Z., Barkoff, D. W., & McCaffrey, D. (2018). The Critical Metals: An Overview and Opportunities and Concerns for the Future. In A.

M. Arribas R. & J. L. Mauk (Eds.), *Metals, Minerals, and Society* (pp. 25–38). Society of Economic Geologists. https://doi.org/10.5382/SP.21.02

Kumar, A., Sanislav, I., Martin, L., Aleshin, M., & Dirks, P. (2024). Genesis of copper mineralization in the polymetallic tin deposits from the Herberton Mineral Field, Queensland, Australia. *Mineralium Deposita*, *59*(2), 291–311. https://doi.org/10.1007/s00126-023-01209-4

Langmuir, D., Mahoney, J., & Rowson, J. (2006). Solubility products of amorphous ferric arsenate and crystalline scorodite (FeAsO4·2H2O) and their application to arsenic behavior in buried mine tailings. *Geochimica et Cosmochimica Acta*, *70*(12), 2942–2956. https://doi.org/10.1016/j.gca.2006.03.006

Lottermoser, B. G., & Ashley, P. M. (2006). Mobility and retention of trace elements in hardpan-cemented cassiterite tailings, north Queensland, Australia. *Environmental Geology*, *50*(6), 835–846. https://doi.org/10.1007/s00254-006-0255-8

Nassar, N. T., Graedel, T. E., & Harper, E. M. (2015). By-product metals are technologically essential but have problematic supply. *Science Advances*, *1*(3), e1400180. https://doi.org/10.1126/sciadv.1400180

Nazari, A. M., Ghahreman, A., & Bell, S. (2017). A comparative study of gold refractoriness by the application of QEMSCAN and diagnostic leach process. *International Journal of Mineral Processing*, *169*, 35–46. https://doi.org/10.1016/j.minpro.2017.10.007

Ryan, C. G., Siddons, D. P., Kirkham, R., Li, Z. Y., De Jonge, M. D., Paterson, D. J., Kuczewski, A., Howard, D. L., Dunn, P. A., Falkenberg, G., Boesenberg, U., De Geronimo, G., Fisher, L. A., Halfpenny, A., Lintern, M. J., Lombi, E., Dyl, K. A., Jensen, M., Moorhead, G. F., … Borg, S. (2014). Maia X-ray fluorescence imaging: Capturing detail in complex natural samples. *Journal of Physics: Conference Series*, *499*, 012002. https://doi.org/10.1088/1742-6596/499/1/012002

Stromberg, J. M., Van Loon, L. L., Gordon, R., Woll, A., Feng, R., Schumann, D., & Banerjee, N. R. (2019). Applications of synchrotron X-ray techniques to orogenic gold studies;

examples from the Timmins gold camp. *Ore Geology Reviews*, *104*(March 2018), 589–602. https://doi.org/10.1016/j.oregeorev.2018.11.015

U.S. Geological Survey. (2025). *Mineral Commodity Summaries* (p. 212). U.S. Geological Survey. https://doi.org/10.3133/mcs2025

Walshe, J. L., Solomon, M., Whitford, D. J., Sun, S.-S., & Foden, J. D. (2011). The role of the mantle in the genesis of tin deposits and tin provinces of eastern Australia. *Economic Geology*, *106*(2), 297–305. https://doi.org/10.2113/econgeo.106.2.297